

Light charged particle production in neutron-induced reactions on aluminum at $E_n = 62.7$ MeV

S. Benck, I. Slypen, and J. P. Meulders

Institut de Physique Nucléaire, Université Catholique de Louvain, Chemin du Cyclotron 2, B-1348 Louvain-la-Neuve, Belgium

V. Corcalciuc

Institute for Atomic Physics, P.O. Box MG6, Bucharest, Romania

M. B. Chadwick and P. G. Young

University of California, Theoretical Division, Los Alamos National Laboratory, Los Alamos, New Mexico 87545

A. J. Koning

Netherlands Energy Research Foundation ECN, BU - Nuclear Energy, P.O. Box 1, 1755 ZG Petten, The Netherlands

(Received 6 April 1998)

Double-differential cross sections for 62.7 ± 1.0 MeV neutron-induced light charged particle (p , d , t , and α) production on aluminum are reported. Angular distributions were measured at laboratory angles between 20° and 160° in steps of 10° . Procedures for data taking and data reduction are described. Results for double-differential, energy-differential, and total production cross sections are presented. The measurements are compared to existing proton-induced data and to nuclear model calculations which include preequilibrium and equilibrium decay mechanisms. Agreement with the model calculations is good for all ejectile types except for deuterons, where pickup processes are overestimated. The neutron-induced data presented are shown to be in good agreement with experimental proton-induced data for charge-symmetric reaction channels. For the proton emission channel the approximate factor of two between the two emission spectrum measurements is explained. [S0556-2813(98)00309-4]

PACS number(s): 25.40.Hs, 28.20.-v

I. INTRODUCTION

Experimental measurements of emission spectra for charged particle production in fast neutron-induced reactions above 14 MeV are rather scarce. The present paper reports the first measurements of proton, deuteron, triton, and α -particle inclusive emission spectra induced by 62.7 MeV neutrons on aluminum. Experimental data were obtained at the fast neutron facility at the Louvain-la Neuve cyclotron CYCLONE. Previous results for neutron induced light charged particle production on carbon in the energy interval 40–75 MeV were reported by our group [1,2].

Neutron-induced reactions on aluminum are of interest for a number of reasons. Aluminum is sufficiently heavy for many of the statistical assumptions used in nuclear reaction models to hold (they frequently rely on a high density of excited states in their derivation), yet not so heavy as to result in a strong suppression of charged particle emission due to the Coulomb barrier. Therefore nuclear reaction models for equilibrium and preequilibrium decay, including the emission of cluster particles, can be tested.

Results concerning light charged particle production in proton induced reactions on aluminum at a comparable energy, 61 MeV, were previously reported [3]. Our data, together with those of Ref. [3], provide comprehensive information of all important light particle decay channels. This allows a comparison of the influence of the projectile isospin on the relative magnitudes of charged particle yields and facilitates a more stringent test of nuclear models. Additionally, experimental measurements of $^{27}\text{Al}(n, x\gamma)$ reactions from 3 to 400 MeV have recently been presented, for the

production of discrete gamma rays in various residual nuclei [4]. These data probe particularly the angular-momentum affects in the nuclear reaction, and indirectly depend on the emission cross sections in the reaction. They are, therefore, complementary to the measurements we report here, and together these measurements provide a comprehensive description of nucleon-induced reactions on aluminum.

The charged particle emission spectra are analyzed using two different preequilibrium reaction theories: the quantum-mechanical Feshbach-Kerman-Koonin (FKK) theory [5] and the semiclassical exciton model. The GNASH nuclear reaction model code [6] predicts emission spectra for all the four ejectiles using the exciton model for preequilibrium emission and Hauser-Feshbach theory for sequential equilibrium decay. Direct inelastic scattering contributions are also included in the GNASH calculations, thus the code provides a comprehensive description of all important reaction channels, albeit in a semiclassical framework for preequilibrium decay. On the other hand, the FKK theory is grounded in a more fundamental theoretical derivation but at present can only be used for nucleon emission. Nevertheless, since quantum refraction and diffraction effects are incorporated within its distorted-wave formalism, the FKK theory can predict the angular distributions of the emitted nucleons.

The present aluminum data enable the test of a recent theoretical formulation of multistep direct reactions [7]. This theory uses the FKK approximations that result in a convolution structure for second- and higher-order scattering processes, and explicitly follows the excitation of nucleons within the preequilibrium cascade. Experimental data for both emitted protons and neutrons (inferred by symmetry

from (p, xp) data of Ref. [3]) enables this theory to be tested. The incident neutron energy of 62.7 MeV has the advantage that the first-particle multistep direct reaction mechanism is dominant, the energy being too high for multistep compound processes and too low for significant multiple preequilibrium emission [8] to become important.

In addition to basic physics interest, neutron-induced reactions above 20 MeV on aluminum are important in a number of emerging accelerator-driven technologies which utilize spallation neutrons, including the transmutation of radioactive waste. An accurate understanding of these cross sections is important for radiation transport calculations of shielding requirements, heating, activation and radiation damage.

In Sec. II the experimental setup and data reduction procedures are briefly presented. Experimental results are shown in Sec. III. In Sec. IV we describe nuclear model calculations of direct, preequilibrium, and equilibrium reaction mechanisms including the FKK theory. Comparisons of our measurements and those of Ref. [3] with the theoretical predictions are shown in Sec. V. Conclusions are given in Sec. VI.

II. EXPERIMENTAL METHODS

The present paper reports experimental data for proton, deuteron, triton, and α -particle production by 62.7 ± 1 MeV neutron-induced reactions on aluminum. Since the experimental setup and data reduction procedures are very similar to those in our previous works, only essential details are given here. For further information the reader is referred to Refs. [1,2] and the references therein.

Figure 1 shows the general layout (not at scale) of the fast neutron beam facility at the Louvain-la-Neuve Cyclotron CYCLONE [9–11]. The 65 MeV proton beam is focused on a 3 mm thick natural lithium target. With a 10^{-5} A proton beam, about 10^6 n/s are available at the location of our reaction chamber. The neutron energy spectrum at 0° consists of a well-defined peak (with full width at half maximum of 2 MeV) containing about 50% of the neutrons, plus a flat continuum of low-energy neutrons [1,11].

The collimated neutron beam strikes the target placed in a first evacuated reaction chamber (406 mm in diameter) coupled to the exit of the neutron collimator (Fig. 1). Laboratory angles from 20° to 160° in steps of 10° were available for measurements [12,13].

Four charged particle detector telescopes were used simultaneously. Each of them consisted of (i) a ΔE detector (NE102 plastic scintillator, 0.1 mm thick, 4 cm in diameter) viewed by a XP2020 photomultiplier via a lucite light guide and (ii) an E detector [CsI(Tl) crystal, 22 mm thick, 38.1 mm in diameter], viewed by a XP2262B photomultiplier. The E detector can stop 80 MeV protons. A coincidence was required between ΔE and E detectors in order to suppress an important part of the background present in such types of experiment [1,11,13]. The average angular opening of the collimating system for the detection of charged particle products was $2^\circ - 3^\circ$.

An aluminum target (5×5 cm² surface and 1 mm thick) was used. The angle of the target with the beam was chosen to minimize the thickness of the target material traversed by the charged particle ejectiles towards the telescopes.

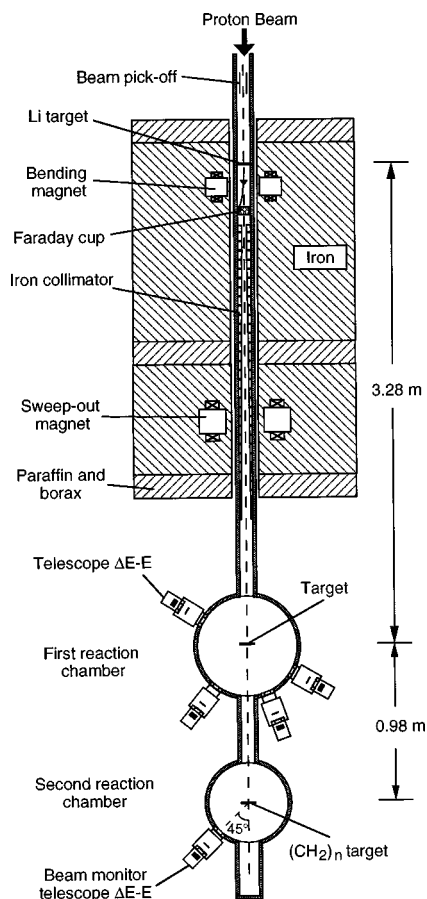


FIG. 1. General layout of the fast neutron facility at the Louvain-la-Neuve Cyclotron CYCLONE.

For the energy calibration, the protons and deuterons recoiling from respectively a polypropylene (1 mm thick) and a deuterated polypropylene target (0.6 mm thick) were used. They were recorded at laboratory angles from 20° to 70° in steps of 10° , for each of the four telescopes used. These measurements provided a reliable energy calibration for protons and deuterons. Together with an α -source point (at about 5.5 MeV), this gives about 13 calibration points. A simple three-parameter analytical formula relates the CsI light output response to the energy of the detected charged particle [14,15]. A simultaneous fit, to all the calibration points, determines the three parameters and therefore the energy calibration for the four ejectiles. Specially for alpha-particles, the errors on the three free parameters induce errors in the energy calibration. Therefore, the energy spectra for triton and α -particle production are reported here as histograms in steps of 3 MeV. In addition, as the measured cross sections for these two ejectiles are rather small, this choice of the energy step improves the statistics in the reported spectra.

Charged particle discrimination spectra were obtained in two ways: (i) by using the energy information from ΔE and E detectors and (ii) by charge integration of the CsI light output pulse [1,16]. A combined use of these two separation methods allows a good separation of the reaction products over their entire energy range as well as an efficient suppression of the background [1,2,11,13]. Nevertheless, due to the poor separation of the ^3He ejectiles in the particle discrimi-

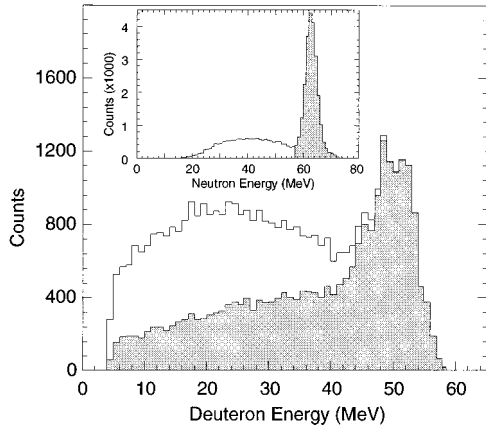


FIG. 2. Selection of deuteron events induced by neutrons in the main peak (hatched area). In the inset the neutron spectrum reconstructed from the totality of deuteron events is shown. The spectra are at 20° lab and the indicated deuteron energy is after the target.

nation spectra, in what follows all the presented experimental α spectra contain as well the ^3He contribution.

The beam monitoring system was realized in two ways. (i) After the lithium target, the incident proton beam is magnetically deflected into a water cooled Faraday cup and then integrated. (ii) Downstream of our reaction chamber and coupled to it, there is a second evacuated chamber (Fig. 1), in which a charged particle telescope detects the $\text{H}(n,p)$ scattered protons at 45° from a 1 mm thick polypropylene target. The agreement between these two monitoring systems was very good during the data taking [1,13].

The time-of-flight (TOF) was deduced from the time difference between a capacitive beam pickoff, located upstream of the neutron producing target (Fig. 1) and the ΔE detector. It was registered for each charged particle event in the telescopes and subsequently used to select only those events associated with neutrons in the main neutron peak [1,2,11,13].

By complementary use of $\Delta E-E$ and slow vs fast component information for the particle discrimination spectra, a reliable selection of the desired events was obtained [1,2,11,13]. Subsequently, using TOF information and knowing the flight distances and energies of the particles (from the energy calibration), a further selection was made for only those events induced by neutrons from the monoenergetic peak. Figure 2 shows, for the case of the $\text{Al}(n,dx)$ reaction, the selection of the deuteron events induced by neutrons in the main peak. The rest of the deuterons (nonhatched area) are induced by neutrons in the low-energy continuum of the incident neutron energy spectrum.

The statistics in our spectra correspond to an acquisition time of about 32 h for forward and 60 h for backward angles, with a mean proton beam intensity of about $12 \times 10^{-6} \text{A}$ on a 3 mm thick lithium target.

Absolute cross sections were obtained by normalization to our measured $\text{H}(n,p)$ scattering cross sections. Angular distributions for the $n-p$ elastic scattering were measured at 6 laboratory angles between 20° and 70° , for each telescope [17]. Solid angles and thick target corrections were calculated with a Monte Carlo simulation program of the experiment [18]. In this way, for each of the telescopes, six normalization points were available covering a large energy

range, and the normalization factor was obtained from their mean value. Generally the spread of these values around the mean was about 5%. Normalization factors of the order of $3-4 \times 10^{-4} \text{mb/MeV sr}$ were obtained, indicative of the detection sensibility of the experiment.

The rather thick aluminum target, the 0.1 mm thick ΔE detector, and the energy threshold of the E detector (about 1.5 MeV), limit the registration of the low-energy charged particle products to only fractions of the entire target thickness, and therefore the spectra should be corrected accordingly. These effects are taken into account by using the abovementioned simulation program [1,18].

Data were archived on workstation disks and on Exabyte tapes for an off-line analysis.

III. EXPERIMENTAL RESULTS

Using the procedures outlined above, double-differential cross sections for proton, deuteron, triton, and α -particle production were obtained for 62.7 MeV incident neutron energy, corresponding to the main neutron peak that results from 65 MeV incident protons on the lithium target. Figures 3–6 show, in three-dimensional (3D) representations, the measured energy spectra and their angular distributions for the four ejectiles. The energy spectra are represented as histograms in steps of 2 MeV for protons and deuterons and 3 MeV for tritons and α particles. The horizontal scale gives the energy of the charged particles produced in the reaction. Low-energy cuts are about 6 MeV for protons and deuterons and about 12 MeV for tritons and α particles. The rather high values of the low-energy cuts in the triton spectra are due to the poor separation of the low energy tritons in the particle identification spectra while for the α -particle spectra they are determined by thick target effects. The angular distributions in Figs. 3–6 show a strong peaking at forward laboratory angles for all the four ejectiles, indicative of the presence of preequilibrium processes.

Given by the accumulated statistics, the overall relative errors of the points in the energy spectra are about 5% for protons, 9% for deuterons, 17% for tritons, and 28% for α particles. For lower ejectile energies they are larger as a result of the thick target effects [1,18]. The uncertainty in the cross section absolute scale is about 6%, given by errors in the measured reference (n,p) cross sections (5%), beam monitoring (2%), statistics in the $\text{H}(n,p)$ recoil proton peak (2%), and solid angle corrections (1%).

IV. THEORETICAL MODELS

A. Quantum multistep direct calculations

A quantum-mechanical analysis has been performed with a recent, two-component, extension [7] of the multistep direct (MSD) model of Feshbach-Kerman-Koonin [5]. It comprises a combination of distorted-wave Born approximation (DWBA) matrix elements and a statistical description of the excited states that tends to account for experimental angle-integrated emission spectra with an accuracy comparable to that found in the semiclassical models, and with a higher accuracy for angular distributions. When a reaction proceeds by the MSD mechanism, it is supposed that at least one particle is in the continuum throughout the process and

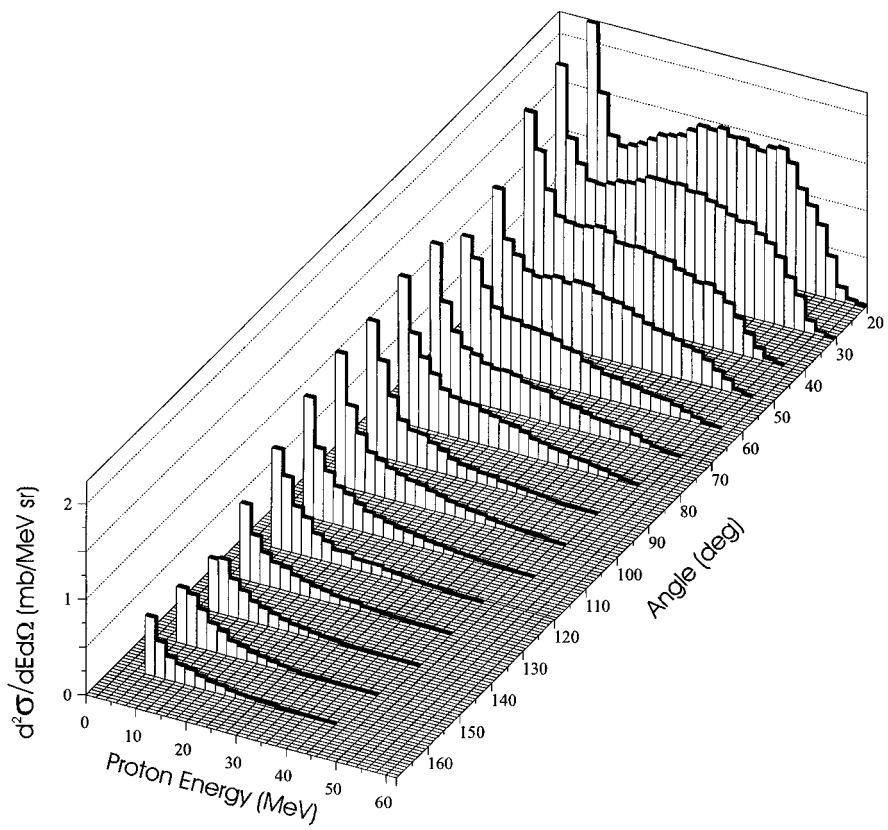


FIG. 3. Angular distribution of measured double-differential cross sections for $^{27}\text{Al}(n,px)$ reactions at 15 laboratory angles (histograms in steps of 2 MeV) for 62.7 MeV incident neutron energy.

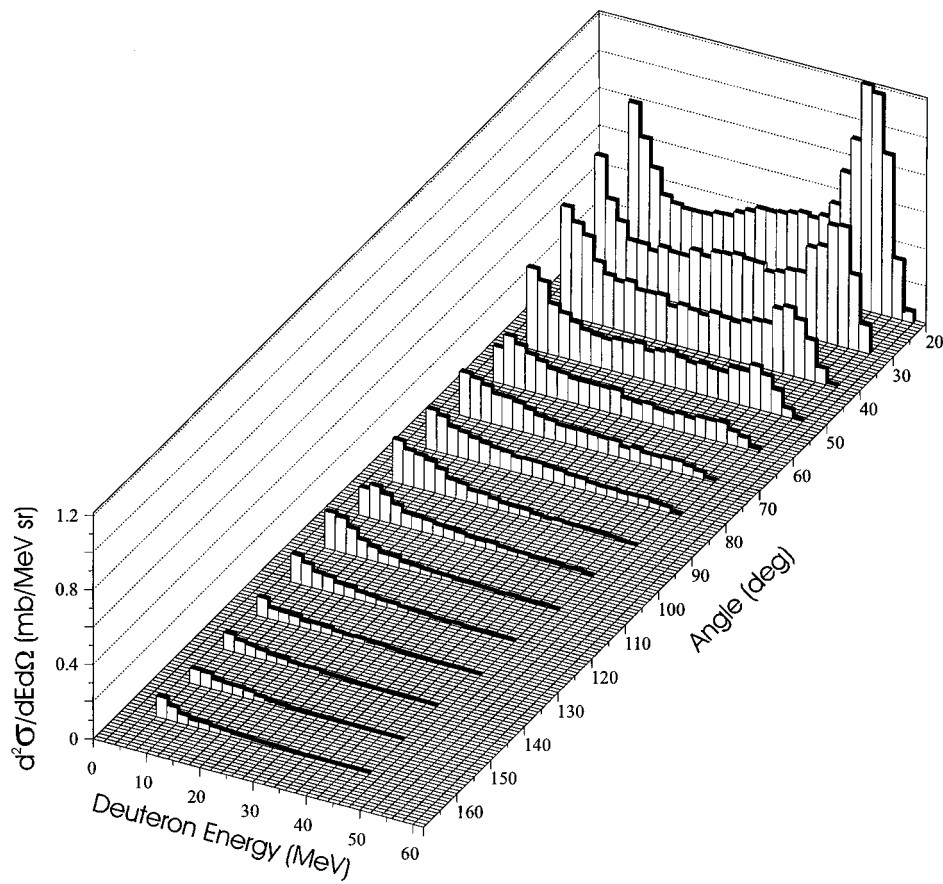


FIG. 4. Same as in Fig. 3 for the case of $^{27}\text{Al}(n,dx)$ reactions.

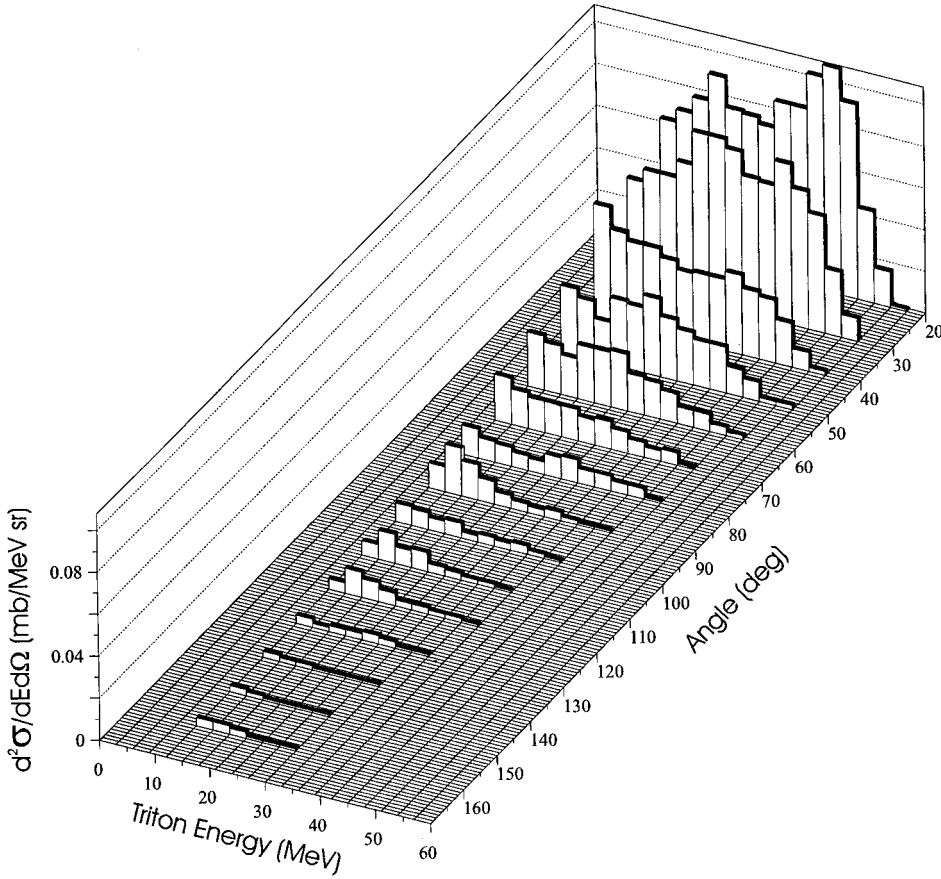


FIG. 5. Angular distributions of measured double-differential cross sections (histograms in steps of 3 MeV) for $^{27}\text{Al}(n,tx)$ reactions at 62.7 MeV incident neutron energy.

that at each subsequent step of the reaction a new particle-hole pair is created. After one or a few collisions, the continuum particle is emitted in a direction that still has retained some coupling to the initial direction and is therefore forward peaked. The main difference with conventional direct reaction theories is the high density of final and intermediate states, which necessitates statistical postulates in the direct reaction formalism so that the analysis of these processes remains tractable. In Ref. [7] we presented a formalism for calculating MSD cross sections in a fully two-component theory where all possible neutron and proton particle-hole excitations are explicitly followed, for all orders of scattering. The best test cases for this model are those where both experimental neutron and proton emission spectra are available, which is always important since these processes represent competing decay channels. Given that (p, xp) emission spectra for aluminum, as measured by Bertrand and Peelle [3], are expected to be similar to (n, xn) spectra at 63 MeV, for emission energies above the Coulomb barrier, the measured (n, xp) data presented in this paper together with the (p, xp) data at the same incident energy provide a stringent test of the theory.

A full exposition of the theory is given in Ref. [7]. Here, we only give the key formulas that were used in the analysis. The double-differential MSD cross section to the continuum is an incoherent sum of a one-step term and multistep terms

$$\frac{d^2\sigma_{j\leftarrow i}(E, \Omega \leftarrow E_0, \Omega_0)}{d\Omega dE} = \sum_{n=1}^{\infty} \frac{d^2\sigma_{j\leftarrow i}^{(n)}(E, \Omega \leftarrow E_0, \Omega_0)}{d\Omega dE}, \quad (4.1)$$

where E_0, Ω_0, i and E, Ω, j are the energy, solid angle, and type of the incident and outgoing nucleon, respectively.

The continuum one-step direct cross section is given by the weighted sum over squared DWBA matrix elements that describe transitions to particle-hole states μ . In a two-component form, it is given by

$$\begin{aligned} \frac{d^2\sigma_{j\leftarrow i}^{(1)}(E, \Omega \leftarrow E_0, \Omega_0)}{d\Omega dE} &= \frac{m^2}{(2\pi\hbar^2)^2} \frac{k}{k_0} \sum_{\mu} \hat{\rho}_{\mu}(p_{\pi}, h_{\pi}, p_{\nu}, h_{\nu}, E_x) \\ &\times |\langle \chi_j^{(-)}(E, \Omega) | \langle \mu(p_{\pi}, h_{\pi}, p_{\nu}, h_{\nu}) | \mathcal{V} | 0 \rangle \\ &\times |\chi_i^{(+)}(E_0, \Omega_0) \rangle|^2, \end{aligned} \quad (4.2)$$

where k and k_0 are the final and initial momentum and $E_x = E_0 - E + Q$ is the excitation energy with Q the reaction Q value. The distorted waves χ are eigenfunctions of the Schrödinger equation with an optical potential. The effective nucleon-nucleon interaction \mathcal{V} manifests itself in $\mathcal{V}_{\pi\pi}$, $\mathcal{V}_{\pi\nu}$ ($=\mathcal{V}_{\nu\pi}$), and $\mathcal{V}_{\nu\nu}$ components. The sum over μ represents a sum over all accessible isospin-dependent particle-hole pairs and $\hat{\rho}_{\mu}$ should be regarded as a probability distribution around each particle-hole state, its width being a measure for the magnitude of the residual interaction within the nucleus. We assume that this distribution can be represented by a Gaussian, and we take a spreading width equal to 4 MeV.

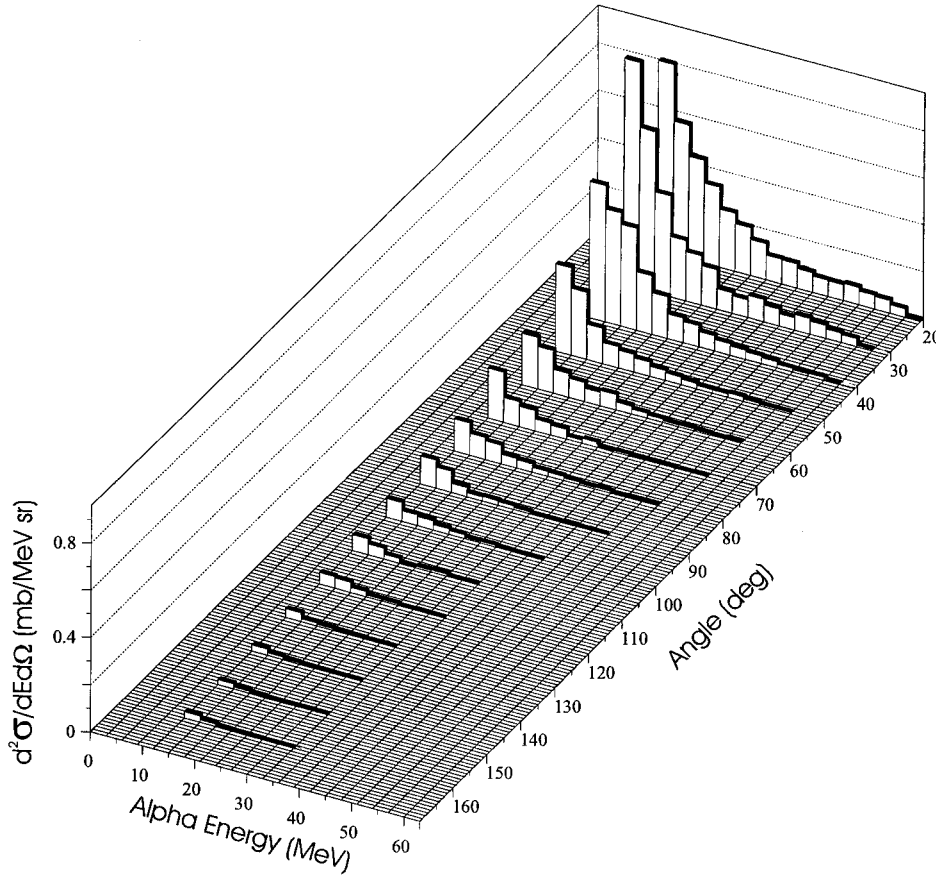


FIG. 6. Same as in Fig. 5 for the case of α -particles.

In general, the n -step direct cross section can be completely expressed in terms of the two-component MSD cross section of the previous stage

$$\begin{aligned} & \frac{d^2 \sigma_{j \leftarrow i}^{(n)}(E, \Omega \leftarrow E_0, \Omega_0)}{d\Omega dE} \\ &= \frac{m}{4\pi^2 \hbar^2 t_{n-1} = \pi, \nu} \sum \int d\Omega_{n-1} \int dE_{n-1} E_{n-1} \\ & \quad \times \frac{d^2 \sigma_{j \leftarrow i}^{(1)}(E, \Omega \leftarrow E_{n-1}, \Omega_{n-1})}{d\Omega dE} \\ & \quad \times \frac{d^2 \sigma_{i_{n-1} \leftarrow i}^{(n-1)}(E_{n-1}, \Omega_{n-1} \leftarrow E_0, \Omega_0)}{d\Omega_1 dE_1}. \end{aligned} \quad (4.3)$$

where E_1, Ω_1 are the intermediate energy and solid angle, respectively. The extra summation over t_{n-1} indicates both types of nucleons that are involved in the intermediate stages.

Equations (4.2), (4.3) are calculated exactly, i.e., we do not make use of explicit formulas for the particle-hole state densities but instead directly calculate DWBA cross sections for all possible particle-hole excitations (again including an exact book keeping of the neutron/proton type of the particle and hole at all stages of the reaction) determined from a simple Nilsson model. Single-particle states for both protons and neutrons were generated, resulting in particle-hole quantum numbers for four types of nucleon-nucleon combina-

tions. For all these states DWBA matrix elements are calculated with the nuclear reaction code ECIS95 [19]. The bound state wave functions are computed with a Woods-Saxon potential with a reduced radius of 1.2 fm and a diffuseness of 0.6 fm. We only consider the real, central term of the effective nucleon-nucleon interaction \mathcal{V}_{ij} , for which we take a Yukawa potential with range $r_0 = 1$ fm and strength V_{ij} . This strength is taken as the only adjustable parameter. The extracted value for the strength of the effective interaction is $V_{\pi\pi} = V_{\nu\nu} = V_{\pi\nu} = 21.1$ MeV, which is in good agreement with the systematical expression found in Ref. [7],

$$V_{\pi\nu} = 31.8 \exp\left(-\frac{0.20}{31.8} E\right) \text{ MeV}, \quad (4.4)$$

where E is the incident energy. We include multiple-preequilibrium emission in the calculations, using the model of Chadwick *et al.* [8].

B. Semiclassical exciton model and Hauser-Feshbach calculations

As discussed above, the FKK theory is able to predict angular distributions as well as emission energy spectra for nucleon ejectiles. However, its predictive capability for the emission of cluster ejectiles (deuterons, tritons, ^3He , and α particles) is limited. A few researchers have begun extending the multistep theory to describe such reactions, but the theory is still in a developmental stage [20]. There exist semiclassical theories, though, which have been developed to describe preequilibrium cluster emission within the exciton

model. For this reason, we also perform calculations that use the exciton model to describe preequilibrium reactions, and Hauser-Feshbach theory to describe the subsequent compound nucleus decay. The GNASH nuclear model code is used for this purpose. The preequilibrium emission of nucleons is calculated by solving a coupled set of master equations to describe the creation and annihilation of particle-hole excitations as the system moves towards equilibrium. Preequilibrium cluster particle emission is calculated using the model of Kalbach [21], which includes pickup and knockout emission mechanisms, making extensive use of phase space and detailed balance considerations to determine the preequilibrium emission rates. In addition to primary preequilibrium emission, multiple preequilibrium emission of a second fast nucleon was included in the calculations [8]. Subsequent compound nucleus decay is calculated in an open-ended sequence of sequential decays, until there is insufficient energy for further particle decay, and the residual nuclei attain their ground states via γ -ray emission.

Hauser-Feshbach calculations require transmission coefficients for particle emission, for energies spanning from zero to the maximum emission energy. The aluminum optical potential of Petler *et al.* [22], fitted to measured elastic scattering and total cross section data, was used for neutrons. For protons, the Petler neutron potential was modified using a Lane isospin transformation. Deuteron transmission coefficients were obtained from the Perey and Perey global potential [23], triton transmission coefficients from the Becchetti-Greenlees potential [24], and α -particle transmission coefficients were obtained from the potential of Arthur and Young [25]. The Ignatyuk model [26] nuclear level densities were used, which include the washing-out of shell effects with increasing excitation energy, and are matched continuously onto low-lying experimental discrete levels, obtained primarily from the compilation of Endt [27].

The semiclassical exciton model, in its form as implemented within the GNASH code, predicts only angle-integrated emission spectra and not angular distributions. This is because the master equations follow particle and hole excitation in energy, but not in momentum space. To obtain double-differential emission spectra, the phenomenological (experimental-data-based) Kalbach angular distribution systematics [28] are applied. While these systematics are phenomenological, theoretical arguments have been presented [29] to support the mathematical form of the systematics, which represent the angular distributions as exponentials in the cosine of the scattering angle.

V. COMPARISON BETWEEN EXPERIMENT AND THEORY

The cross sections in Figs. 3–6 can be compared with the corresponding experimental proton induced reactions on aluminum at 61 MeV incident energy by Bertrand and Peelle [3] and the results from theoretical model calculations described in the previous section. Figure 7 shows measured angular distributions for inclusive proton emission for emission energies of 15, 25, 35, 45, and 51 MeV. Theoretical prediction based on the quantum multistep FKK theory are shown as dotted lines; exciton model predictions combined with the Kalbach angular distribution systematics are shown

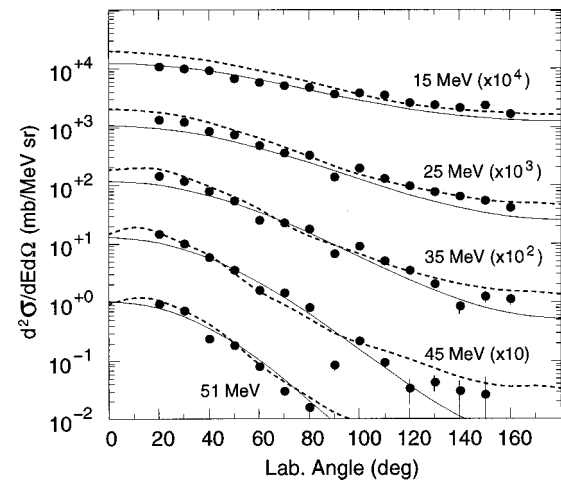


FIG. 7. Angular distributions of laboratory double-differential cross sections for several proton ejectile energies for the $^{27}\text{Al}(n,px)$ reactions at 62.7 MeV incident neutron energy. Continuous and dotted lines show respectively the GNASH code and FKK model calculations of the present work.

as continuous lines. Both model calculations account for the experimental data rather well, including the increased forward peaking with emission energy. At the lower emission energies the contribution from multistep scattering reactions, as opposed to one step direct reactions, increases, which gives a flatter angular distribution.

Figures 8–11 show measured double-differential emission spectra compared with calculations, for proton, deuteron, triton, and α -particle ejectiles, respectively. Data at various emission angles are presented. As our two-component development to the FKK theory is currently capable only of predicting nucleon emission cross sections, such calculations are only included in Fig. 8.

The GNASH model calculations shown as the continuous line in Fig. 8 account for the general features exhibited by measurements, that is, the high-energy tail due to preequilibrium emission, the rise at low energies due to contributions

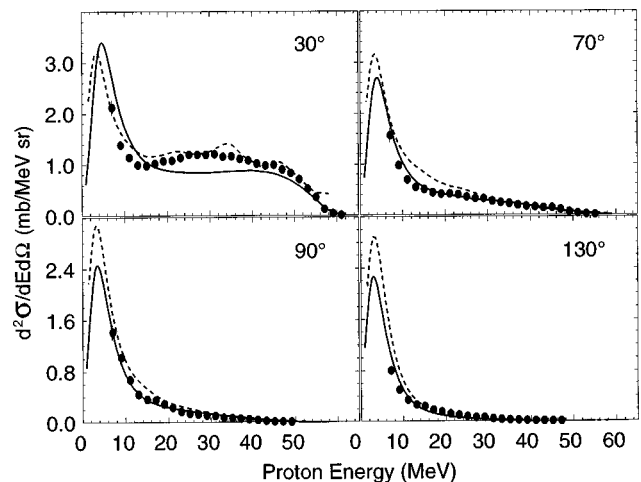


FIG. 8. Measured double-differential cross sections in steps of 2 MeV at several laboratory angles (filled dots) for $^{27}\text{Al}(n,px)$ reactions for 62.7 MeV incident neutron energy. Continuous lines show theoretical calculations with exciton (GNASH) model. Theoretical predictions of the FKK model are presented as dotted lines.

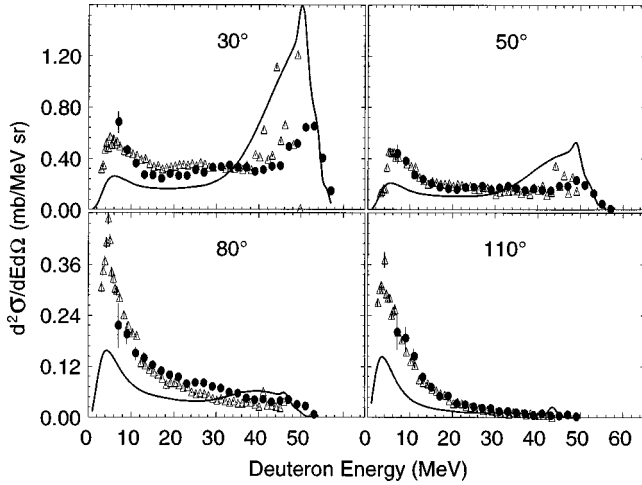


FIG. 9. Measured double-differential cross sections in steps of 2 MeV at several laboratory angles (filled dots) for $^{27}\text{Al}(n,d,x)$ reactions at 62.7 MeV incident neutron energy. Continuous lines are theoretical calculations of the present work. Data of Ref. [3] for $^{27}\text{Al}(p,d,x)$ reactions at 61.0 MeV incident neutron energy are shown as open triangles.

from sequential compound nucleus decay, and the forward peaking of the data. The slight forward peaking seen even in the equilibrium-decay region at low energies is due to the fact that these data are in the laboratory frame, and the center-of-mass to laboratory kinematical transformation is significant for such a light target nucleus. However, an underprediction of the experimental emission spectra by the exciton model in GNASH occurs between approximately 20 and 40 MeV emission energies. Here the FKK calculations better describe the data, though the slight oscillatory structure that persists in the FKK calculations, due to the use of single-particle states in the calculations, is not seen in the measurements. This indicates that the residual interactions may spread and fragment the single-particle states over a wider energy than included in the calculations.

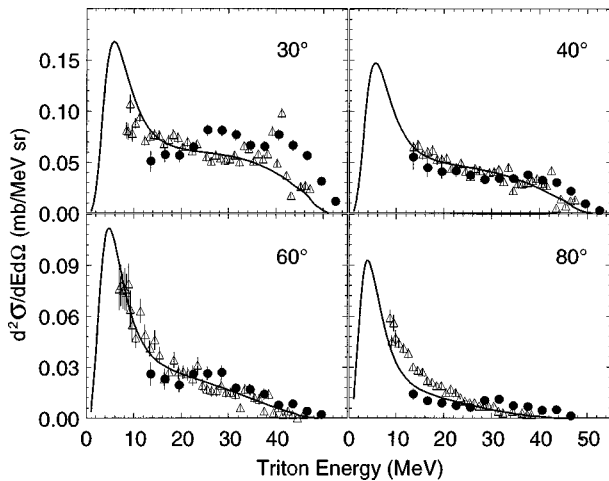


FIG. 10. Measured double-differential cross sections in steps of 3 MeV at several laboratory angles (filled dots) for $^{27}\text{Al}(n,t,x)$ reactions at 62.7 MeV incident neutron energy. Continuous lines are theoretical calculations of the present work. Data of Ref. [3] for $^{27}\text{Al}(p,^3\text{He},x)$ reactions at 61.0 MeV incident neutron energy are shown as open triangles.

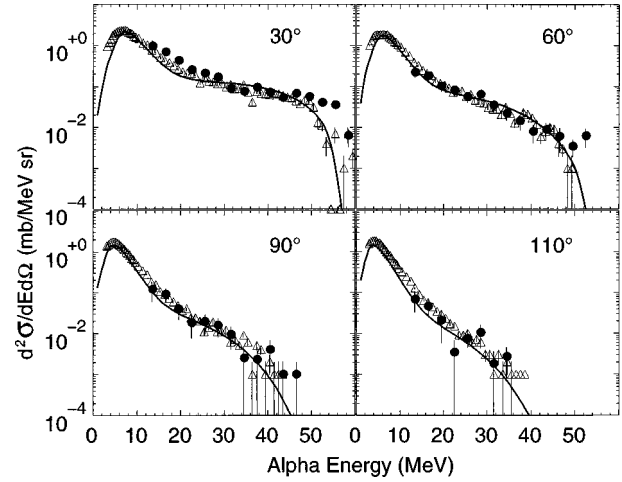


FIG. 11. Measured double-differential cross sections in steps of 3 MeV at several laboratory angles (filled dots) for $^{27}\text{Al}(n,\alpha,x)$ reactions at 62.7 MeV incident neutron energy. Continuous lines are theoretical calculations of the present work. Data of Ref. [3] for $^{27}\text{Al}(p,\alpha,x)$ reactions at 61.0 MeV incident neutron energy are shown as open triangles.

Figures 9–11 show similar information for complex particle emission. Open symbols on the same figures show charge-symmetric data from the proton-induced measurements of Bertrand and Peelle [3]: our (n,xd) , (n,xt) , and $(n,x\alpha)$ data are compared with respectively their (p,xd) , $(p,x^3\text{He})$, and $(p,x\alpha)$ data. In general, remarkable consistency is seen between our neutron-induced charged-particle production cross sections and the symmetric experimental proton-induced cross sections of Ref. [3], particularly when the differing Q values are taken into account. For instance, the differing end points in the spectra are simply due to the slightly different incident energies in the two experiments (62.7 versus 61.0 MeV in Ref. [3]) and the differing Q values [e.g., -6.0 MeV for the (n,d) reaction versus -10.8 MeV for the (p,d) reaction in Fig. 9, and an analogous effect in Fig. 10].

The theoretical calculations using the GNASH code, based on Kalbach's exciton model for the complex particle emission, agree poorly with the deuteron data in Fig. 9, but exhibit better agreement with the triton and α data (Figs. 10,11). In the case of deuteron emission, the model largely overpredicts direct pickup processes at the highest emission energies, and underpredicts compound nucleus deuteron emission. However, the prediction of cluster preequilibrium emission is notoriously difficult for theory, and few theoretical approaches have a good predictive capability for this type of reaction. The failure of theory to account for the experimental deuteron emission data illustrates the need for experimental data to understand these reactions; indeed, in applications the contributions from deuteron emission to energy deposition by neutrons in matter is significant, being only a factor of approximately 3 smaller than protons at this energy.

In the case of α emission (Fig. 11), the model calculations account for the data very well, including the evaporation peak at low energies. Nevertheless, since the detector energy threshold for α emission is rather high in this experiment, much of the α production remains unmeasured. Therefore

the present data cannot be used to test the model calculation predictions of low-energy α emission from compound nucleus reactions. However, the experimental data measuring discrete γ -ray emission following particle emission in neutron reactions on aluminum, described in Ref. [4], can be used indirectly to test the α production calculations at these energies. The model calculations presented in Ref. [4] are compatible with those in the present work—they use the same GNASH code and similar input parameters. The γ -ray cross sections in Ref. [4], which are closely related to residual isotope production cross sections, sum over all the various reaction pathways that contribute to the production of a given isotope. Thus the fact that the model calculations describe measured discrete γ -ray cross sections in $^{20,21,22,23}\text{Ne}$ and in ^{18}F , where an α particle is often emitted in conjunction with other nucleons, supports the accuracy of our model calculations of α emission. The calculations in Ref. [4] exhibit poor agreement with γ -ray data for the production of ^{23}Na at high neutron energies, but at lower energies where energetics dictate that it is α emission as opposed to sequential nucleon emission that is occurring, the calculations agree well with the measurements.

The experimental α spectra contain the contribution due to ^3He ejectiles which is not taken into account in the GNASH theoretical calculations shown in this work, because of their minor importance. Nevertheless, theoretical estimations of these contributions with GNASH show that they are very small compared to the α production cross sections being within the errors of the experimental α production cross sections.

Experimental energy-differential cross sections result from the angle integration of the measured angular distribution of the energy spectra ($d^2\sigma/d\Omega dE$). For a better coverage of the 0° – 180° angular range, cross sections for 2.5° , 10° , 170° , and 177.5° were included. They result from the extrapolation of a fit to the angular distribution, for each ejectile energy, with the simple analytical formula $A \exp(B \cos\theta)$, where A and B are coefficients to be determined by the fit. This functional form is that embodied in the Kalbach systematics for preequilibrium reactions [28] and has been derived theoretically by Chadwick and Oblozinsky [29]. Generally this formula describes the measured angular distributions well over the entire ejectile energy range for all the four ejectiles. This fact gives confidence in our extrapolations for the abovementioned laboratory angles. Moreover, due to the multiplication with $\sin\theta$, in the angle integration, their contribution in the energy-differential cross sections is reduced to about 9%, out of which about 7.5% is due to the cross sections at 10° lab. Figure 12 shows the double-differential cross sections for the four ejectiles at 10° lab. The error bars correspond to the overall relative errors on the energy spectra for each particle as given in Sec. III. The filled points result from the extrapolation with the abovementioned formula, the open triangles are data for 12° lab angle from Ref. [3], for proton induced reactions at 61.0 MeV. The continuous lines are GNASH code predictions. For protons the FKK model calculations are shown as dotted lines. The agreement between the two sets of experimental data in Fig. 12 is good. The general trend of the agreement between the theory and the data, observed at other forward angles (Figs. 8–11) is also seen in Fig. 12.

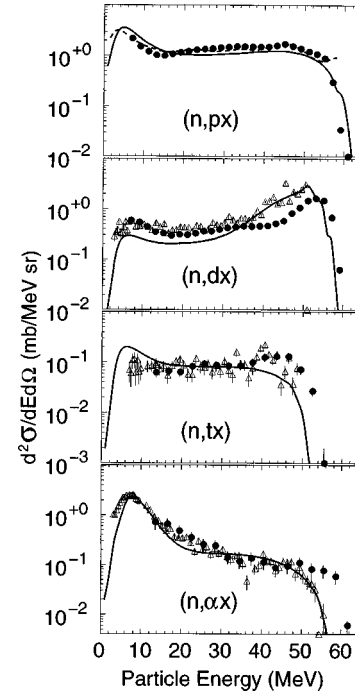


FIG. 12. Double-differential cross sections at 10° lab angles for the four ejectiles (filled points) as they result from our extrapolation. The open triangles are data of Ref. [3] for proton-induced reactions on aluminum at 61.0 MeV. Continuous lines are theoretical model predictions (GNASH) of the present work. For protons, the FKK model calculations are shown as dotted line.

Similar comparisons for the angle-integrated data are shown in Figs. 13 and 14. Again, the good agreement between theory and experiment is evident for all emission channels except deuterons, and the good agreement between the present neutron-induced data and the Bertrand and Peelle proton-induced charge-symmetric data is evident.

Figure 13 shows our energy-differential (n, xp) cross sec-

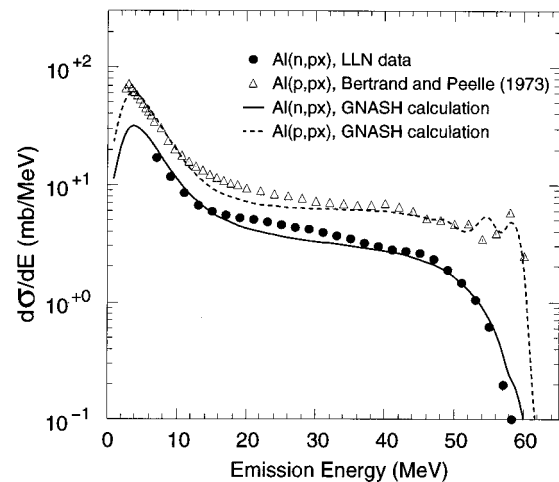


FIG. 13. Experimental energy-differential cross sections for, respectively, $^{27}\text{Al}(n,px)$ reactions at 62.7 MeV incident neutron energy (filled dots) and $^{27}\text{Al}(p,px)$ reactions at 61.0 MeV incident proton energy (open triangles) from Ref. [3]. Continuous and dotted lines show the corresponding model (GNASH) calculations of the present work.

tions compared to Bertrand and Peelle's (p, xp) reaction data, along with model calculations. In this case, the two measurements would not be expected to be of the same magnitude as they are not charge symmetric. In fact, the approximate factor of 2 difference in the preequilibrium region between the proton-induced and neutron-induced data is to be expected from arguments analogous to those proposed by Kalend *et al.* [30]. In a preequilibrium reaction, the first interaction results in the creation of a $2p1h$ state. If one assumes that the projectile is most likely to interact with the opposite type of nucleon, and uses a ratio of 3 compared to the excitation of the same type of nucleon (based on free nucleon-nucleon cross sections), then one obtains a ratio of 5:3 for the number of same-type compared to opposite type excited particles in the first step. Since one-step scattering is the major contributor to the preequilibrium spectrum at this incident energy, this provides a qualitative explanation of the factor of approximately two observed experimentally. The GNASH calculations for neutron- and proton-induced reactions include this effect and account for the two sets of data well. They also account for the preponderance of high-energy protons due to inelastic scattering to low-lying levels in (p, p') reactions, calculated with DWBA theory.

The differing magnitudes of proton emission in the low-energy evaporation region in Fig. 13 has a different origin, more related to Q values. The primary ejectile Q value is -1.8 MeV for the (n, p) reaction, but zero for the (p, p') reaction. This implies that in compound nucleus emission the residual nucleus in the (p, p') reaction is excited at 1.8 MeV higher excitation energy compared to that in the (n, p) reaction, for the same emission energy. Since the emission probability is proportional to the residual nucleus level density, which increases exponentially with excitation energy, this results in a higher proton emission compound nucleus cross section for the proton-induced reaction. However, it must be admitted that other factors also impact on the differing compound nucleus spectrum peaks in Fig. 13, including Q values for other compound nucleus sequential decay contributions, as well as differing competition decay channels in the two cases. For instance, the primary competition decay channel is neutron emission, which has a zero Q value for (n, n') but a -5.6 MeV Q value for the (p, n) reaction, resulting in a higher neutron competition width for the neutron-induced reaction, and thus a smaller proton compound nucleus emission for the neutron-induced reaction.

Similar comparisons of angle-integrated data for all ejectile types are shown in Fig. 14. Again, the good agreement between theory and experiment is evident for all emission channels except deuterons, and the good agreement between the present neutron-induced data and the Bertrand and Peelle proton-induced charge-symmetric data is evident.

Table I gives the total cross sections for proton, deuteron, triton, and α -particle production, resulting from the integration of the experimental energy-differential cross sections in Fig. 14. Theoretical values from model calculations (GNASH) are also shown for comparison. The column labeled theory (1) gives the values resulting from energy integration above the experimental low-energy cuts. The last column, labeled theory (2), gives the theoretical total cross sections under our experimental low-energy cuts (6 MeV for protons and deuterons and 12 MeV for tritons and α particles) and indicates

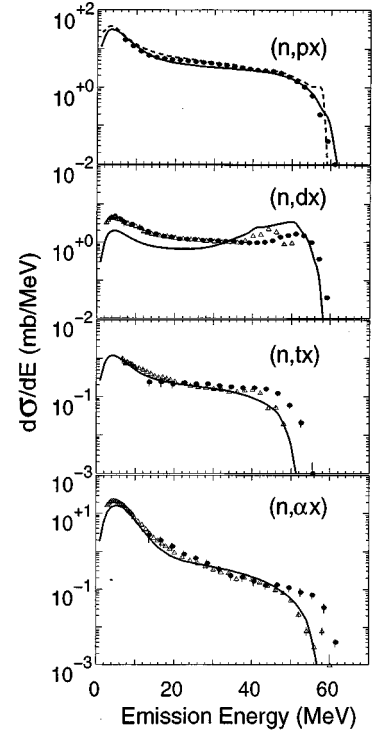


FIG. 14. Experimental energy-differential cross sections for respectively (n, px), (n, dx), (n, tx), and ($n, \alpha x$) reactions on ^{27}Al at 62.7 MeV incident neutron energy (filled dots). The open triangles are data of Ref. [3] for the corresponding 61.0 MeV proton-induced reactions. Continuous lines show the model (GNASH) calculations. For the $^{27}\text{Al}(n, px)$ reactions the dotted line presents the FKK model predictions.

a theoretical estimation of the missing total cross sections in the experiment. The values in the two first columns in Table I agree within the experimental errors.

VI. CONCLUSIONS

We report here, for the first time, proton, deuteron, triton, and α -particle production energy spectra ($d^2\sigma/d\Omega dE$) resulting from the interaction of 62.7 MeV neutrons with aluminum. Measurements were performed with good statistics at the fast-neutron facility of the Louvain-la-Neuve Cyclotron, Belgium. Angular distributions were measured at laboratory angles between 20° and 160° in steps of 10° . Energy-

TABLE I. Total cross sections for proton, deuteron, triton, and α -particle production induced by 62.7 MeV neutrons on aluminum. Theoretical total cross sections (GNASH) are shown for, respectively, above [theory(1)] and under [theory(2)] the experimental low-energy cuts.

	Experiment	Theory (1)	Theory (2)
$\sigma(n, px)$ (mb)	230.5 ± 11.3	230.4	139.2
$\sigma(n, dx)$ (mb)	71.8 ± 6.6	73.0	8.0
$\sigma(n, tx)$ (mb)	7.3 ± 1.3	6.0	8.7
$\sigma(n, \alpha x)$ (mb)	28.4 ± 8.1	22.2	114.2

differential cross sections are deduced from the measured double-differential cross sections.

Overall, these data compare rather well with previously reported measurements of proton-induced reactions on aluminum at 61.0 MeV [3]. Given the lack of neutron-induced experimental data above approximately 14 MeV, the consistency between neutron-induced and proton-induced data for charge-symmetric reaction channels is important, for it means that in the absence of neutron-induced data, proton-induced data can be used to test and guide nuclear model calculations. This is particularly relevant to a number of emerging accelerator-driven technologies which require evaluated neutron-, as well as proton-induced data at high energies. Our calculations using both classical and quantum-mechanical preequilibrium and equilibrium emission theories

describe the experimental data well, except for deuteron emission.

Only illustrative examples of detailed experimental results have been presented here. Complete double-differential and energy-differential cross sections may be obtained, in numerical form, from S.B.

ACKNOWLEDGMENTS

We thank the Louvain-la-Neuve Cyclotron staff for their continual assistance and for the quality of the beam. We acknowledge support from the Institut Interuniversitaire des Sciences Nucléaires, Belgium, from the European Economic Community (contract FI4P-CT95-0024), and from the U.S. Department of Energy.

-
- [1] I. Slypen, V. Corcalciuc, and J.-P. Meulders, *Phys. Rev. C* **51**, 1303 (1995).
- [2] I. Slypen, V. Corcalciuc, J.-P. Meulders, and M. B. Chadwick, *Phys. Rev. C* **53**, 1309 (1996).
- [3] F. E. Bertrand and R. W. Peelle, *Phys. Rev. C* **8**, 1045 (1973).
- [4] A. Pavlik, H. Hitzenberger-Schauer, H. Vonach, M. B. Chadwick, R. C. Haight, R. O. Nelson, and P. G. Young, *Phys. Rev. C* **57**, 2416 (1998).
- [5] H. Feshbach, A. Kerman, and S. Koonin, *Ann. Phys. (N.Y.) (N.Y.)* **125**, 429 (1980).
- [6] P. G. Young, E. D. Arthur, and M. B. Chadwick, Los Alamos National Laboratory Report No. LA-MS-12343, 1992.
- [7] A. J. Koning and M. B. Chadwick, *Phys. Rev. C* **56**, 970 (1997).
- [8] M. B. Chadwick, P. G. Young, D. C. George, and Y. Watanabe, *Phys. Rev. C* **50**, 996 (1994).
- [9] A. Bol, P. Leleux, P. Lipnik, P. Macq, and A. Ninane, *Nucl. Instrum. Methods Phys. Res.* **214**, 169 (1983).
- [10] C. Dupont, P. Leleux, P. Lipnik, P. Macq, and A. Ninane, *Nucl. Instrum. Methods Phys. Res. A* **256**, 197 (1987).
- [11] I. Slypen, Ph.D. thesis, Université Catholique de Louvain, 1995.
- [12] I. Slypen, V. Corcalciuc, and J. P. Meulders, *Rom. J. Phys.* **38**, 431 (1993).
- [13] I. Slypen, V. Corcalciuc, A. Ninane, and J. P. Meulders, *Nucl. Instrum. Methods Phys. Res. A* **337**, 431 (1994).
- [14] D. Horn, C. G. Ball, A. Galindo-Uribarri, E. Hagberg, R. B. Walker, R. Laforest, and J. Pouliot, *Nucl. Instrum. Methods Phys. Res. A* **321**, 273 (1992).
- [15] F. Benrachi, B. Chambon, B. Cheynis, D. Drain, C. Pastor, D. Seghier, K. Zaid, A. Giorni, D. Heuer, A. Llhres, C. Morand, P. Stassi, and J. B. Viano, *Nucl. Instrum. Methods Phys. Res. A* **281**, 137 (1989).
- [16] J. Alarja, A. Dauchy, A. Giorni, C. Morand, E. Pollaco, P. Stassi, R. Billery, B. Chambon, B. Cheynis, D. Drain, and C. Pastor, *Nucl. Instrum. Methods Phys. Res. A* **242**, 352 (1986).
- [17] S. Benck, I. Slypen, V. Corcalciuc, and J.-P. Meulders, *Nucl. Phys.* **A615**, 220 (1997).
- [18] I. Slypen, V. Corcalciuc, and J.-P. Meulders, *Nucl. Instrum. Methods Phys. Res. B* **88**, 275 (1994).
- [19] J. Raynal, *Notes on ECIS94*, CEA Saclay Report No. CEA-N-2772, 1994.
- [20] A. A. Cowley, G. J. Arendse, J. W. Koen, W. A. Richter, J. A. Stander, G. F. Steyn, P. Demetriou, P. E. Hodgson, and Y. Watanabe, *Phys. Rev. C* **54**, 778 (1996).
- [21] C. Kalbach, *Z. Phys. A* **283**, 401 (1977).
- [22] J. S. Petler, M. S. Islam, R. W. Finlay, and F. S. Dietrich, *Phys. Rev. C* **32**, 673 (1985).
- [23] C. M. Perey and F. G. Perey, *At. Data Nucl. Data Tables* **17**, 1 (1976).
- [24] F. D. Becchetti and G. W. Greenlees, in *Proceedings of Conference on Polarization Phenomena in Nuclear Reactions*, edited by H. H. Barschall and W. Haerberli (University of Wisconsin Press, Wisconsin, 1971), Vol. 223, p. 682.
- [25] E. D. Arthur and P. G. Young, "Evaluation of Neutron Cross Sections to 40 MeV for $^{54,56}\text{Fe}$," in *Proceedings of the Symposium on Neutron Cross Sections from 10 to 50 MeV*, Brookhaven National Laboratory, Upton, NY, 1980, edited by M. R. Bhat and S. Pearlstein, Brookhaven National Laboratory Report No. BNL-NCS-51245, 1980, Vol. II, p. 731.
- [26] A. V. Ignatyuk, G. N. Smirenkin, and A. S. Tishin, *Sov. J. Nucl. Phys.* **21**, 255 (1975).
- [27] P. M. Endt, *Nucl. Phys.* **A521**, 1 (1990).
- [28] C. Kalbach, *Phys. Rev. C* **37**, 2350 (1988).
- [29] M. B. Chadwick and P. Oblozinsky, *Phys. Rev. C* **50**, 2490 (1994).
- [30] A. M. Kalend *et al.*, *Phys. Rev. C* **28**, 105 (1983).